Chemical Science

ROYAL SOCIETY OF CHEMISTRY

EDGE ARTICLE

View Article Online
View Journal | View Issue

Cite this: *Chem. Sci.*, 2026, **17**, 5972

All publication charges for this article have been paid for by the Royal Society of Chemistry

Heterogeneous photocatalytic C4 remote fluorosulfonamidation of pyridines

Panjie Xiang,[a] Kai Sun, *[a] Xiaolan Chen, *[a] Kang Li,[ab] Xi Chen,[c] Yunkai Zhang,[a] Lingbo Qu[ac] and Bing Yu *[a]

N-Fluorosulfamoyl pyridinium salts have been ingeniously developed as redox-active precursors for generating fluorosulfamoyl radicals. However, the ubiquitous pyridine scaffold within these compounds, commonplace in numerous pharmaceuticals, has remained being wasted in reported methods only as a radical leaving group. This underutilization presents both a significant challenge and an exciting opportunity for further research in synthetic, medicinal, and materials chemistry. Herein, *N*-fluorosulfamoyl pyridinium salts were employed as bifunctional reagents to achieve remote and selective C–H functionalization of pyridines through a radical relay process that enables polarity reversal of radical intermediates. By employing $ZnIn_2S_4$ as a heterogeneous photocatalyst, this protocol enables the mild and efficient incorporation of both fluorosulfamoyl and pyridyl groups into alkenes, affording synthetically valuable fluorosulfamoyl pyridine derivatives in moderate to good yields. These transformations feature broad substrate scope, good functional group tolerance, and their synthetic utility is further demonstrated through late-stage functionalization of complex bio-relevant molecules. Importantly, the $ZnIn_2S_4$ photocatalyst displays exceptional recyclability, retaining high catalytic efficiency over five consecutive cycles. This work represents the first successful application of a heterogeneous photocatalyst compatible with *N*-fluorosulfamoyl pyridinium salts and *N*-aminopyridinium salts, effectively overcoming the longstanding challenge of catalyst recovery encountered in previous systems.

Received 3rd November 2025
Accepted 21st January 2026

DOI: 10.1039/d5sc08495d

rsc.li/chemical-science

Introduction

Since the introduction of sulfur(VI) fluoride exchange (SuFEx) reactions by Sharpless and coworkers,[1] sulfonyl fluorides have rapidly gained prominence as highly valuable "clickable" reagents.[2] The unique reactivity–stability balance provided by the S–F bond imparts sulfonyl fluorides with rapid and selective nucleophilic reactivity, while simultaneously maintaining exceptional stability under aqueous and physiological conditions.[3] The exceptional characteristics confer sulfonyl fluorides with unparalleled versatility, establishing them as indispensable tools not only for the synthesis and modification of small molecules,[4] polymers,[5] and advanced materials,[6] but also for the intricate rational design of selective enzyme inhibitors and activity-based probes (Fig. 1a).[7] Despite their remarkable potential, the broader application of sulfonyl fluorides has been limited by the restricted diversity and accessibility of sulfonyl fluoride scaffolds, highlighting the urgent need for novel and efficient synthetic strategies to expand the SuFEx toolbox.[8]

Pyridines and related nitrogen-containing heterocycles are widely present in biologically active compounds, with pyridine ranking as the most abundant heteroaromatic ring among FDA-approved medications (Fig. 1a).[9] In recent years, visible-light-driven photoredox catalysis has significantly advanced the construction of complex molecular frameworks, exploiting unique redox pathways to generate value-added molecules under mild and sustainable conditions.[10] In this context, the Minisci reaction, which involves the addition of carbon-centered nucleophilic radicals to protonated azines, remains a fundamental method for functionalizing pyridines (Fig. 1b, path (i)). However, this reaction often faces challenges due to competing regioselectivity at the C2 and C4 positions. For photocatalytic C4 derivatization, pyridines substituted with 4-cyano or 4-triphenylphosphonium groups are particularly prone to *ipso* substitution after undergoing single-electron reduction (Fig. 1b, path (ii)). Alternatively, C4-selective functionalization can be achieved by introducing a blocking group on the nitrogen of the pyridine, effectively directing the subsequent Minisci-type transformation (Fig. 1b, path (iii)).[11] Despite advancements in the field, the photochemical C4 functionalization of pyridine remains underexplored.

[a]*College of Chemistry, Zhengzhou University, Zhengzhou 450001, China. E-mail: sunkaichem@zzu.edu.cn; chenxl@zzu.edu.cn; bingyu@zzu.edu.cn*

[b]*National Engineering Research Center of Low-Carbon Processing and Utilization of Forest Biomass, Nanjing Forestry University, Nanjing 210037, China*

[c]*Institute of Chemistry, Henan Academy of Sciences, Zhengzhou 450002, China*

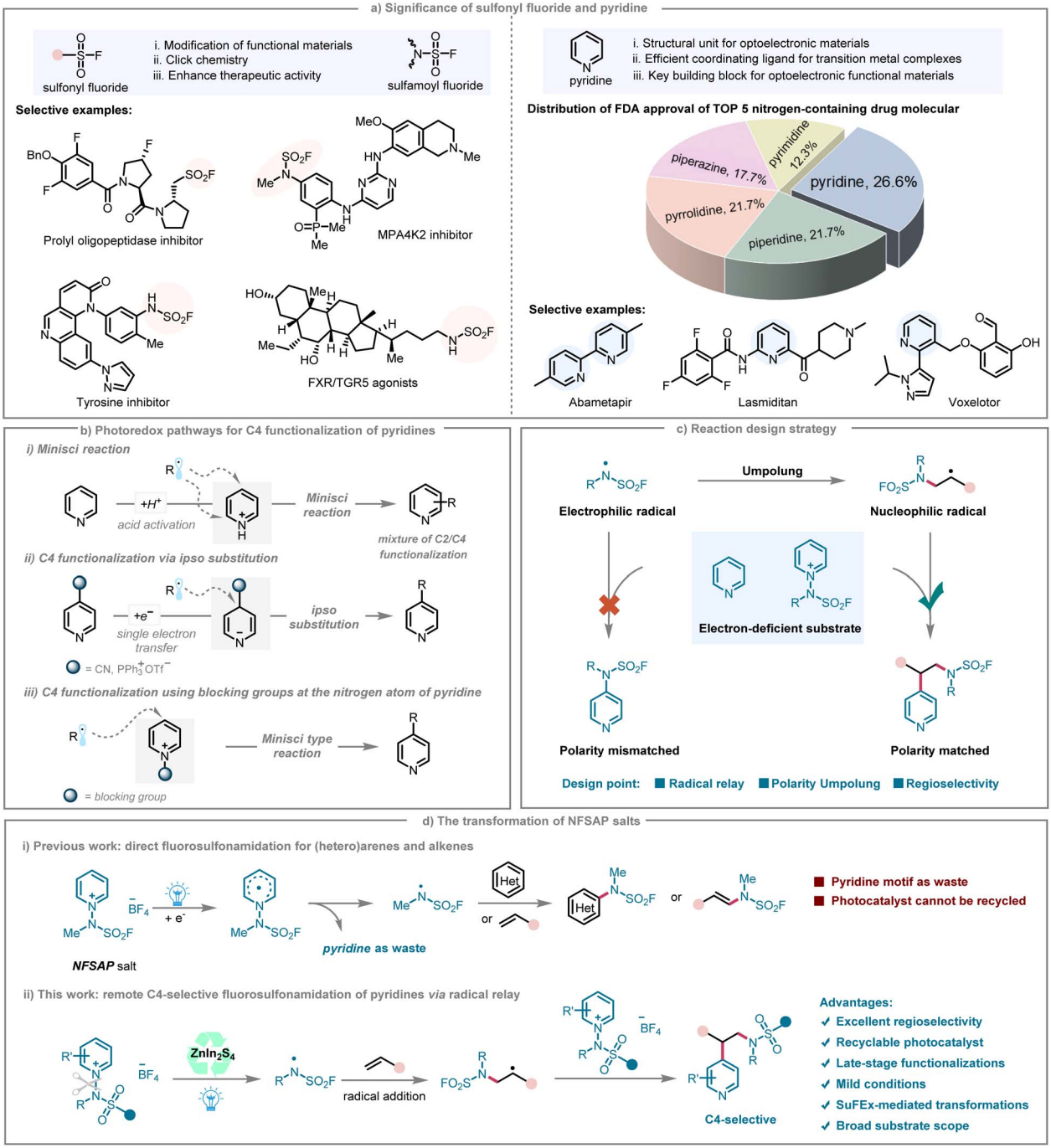

Fig. 1 (a) Significance of sulfonyl fluoride and pyridine; (b) photoredox pathways for C4 functionalization of pyridines; (c) reaction design strategy; (d) the transformation of NFSAP salts.

Driven by the privileged role of sulfamoyl fluorides in drug discovery and the ubiquity of pyridine cores in functional materials, we set out to develop a site-selective, radical-based fluorosulfonamidation of pyridines that proceeds through pyridinium salts (Fig. 1c). The endeavor confronts a fundamental polarity paradox: the N-centered fluorosulfonamidyl radical ($^{\bullet}NSO_2F$) is intrinsically electrophilic and therefore favors electron-rich partners, whereas pyridine, whether neutral or in its cationic salt form, is rendered electron-deficient by the strongly electron-withdrawing nitrogen atom.[12] This electrophilic-radical/electron-poor-substrate mismatch erects a formidable thermodynamic barrier to conventional direct radical addition.[13] To address this issue, we proposed a radical relay strategy to achieve dynamic polarity inversion of the radical species: first converting the electrophilic $^{\bullet}NSO_2F$ radical into a nucleophilic C-centered radical, which then selectively reacts with the electron-deficient pyridinium salt. In recent years, independent reports by the groups of Wang,[14] Liao,[15] and

Weng[16] employed *N*-fluorosulfamoyl pyridinium salts (NFSAPs) as robust and efficient photoredox-active precursors for generating fluorosulfamoyl radicals, thereby enabling direct radical fluorosulfonamidation of alkenes and heterocycles (Fig. 1d, path (i)). However, the pyridine motif embedded within NFSAPs has been largely underutilized in reported transformations, typically serving only as a transient radical leaving group, rather than being incorporated into the target molecules. Furthermore, existing photocatalytic methodologies predominantly rely on homogeneous transition metal complexes or organic dyes as visible-light absorbers.[17] These homogeneous photoredox catalysts frequently suffer from limited compatibility with highly acidic or basic media, strong nucleophiles, electrophiles, or highly reactive radical intermediates, thereby restricting their utility in diverse synthetic settings.[18] Additionally, challenges associated with recycling and reusing these catalysts remain unsolved, substantially hindering their potential in sustainable chemical synthesis.

In contrast, heterogeneous catalysts offer several compelling advantages, including facile separation from the reaction medium, enhanced recyclability, and a reduced risk of catalyst contamination in the final products.[19] These attributes are particularly advantageous for large-scale and sustainable processes, where catalyst recovery and reusability are critical considerations.[20] Among heterogeneous photocatalysts, metal–sulfur compounds, particularly indium zinc sulfide ($ZnIn_2S_4$), have attracted considerable attention, owing to their favorable attributes such as non-toxicity, strong visible-light absorption, appropriate bandgap structure, and tunable morphology. Inspired by these advantages, we employed NFSAPs as bifunctional reagents that simultaneously supply the aminosulfonyl fluoride motif and the pyridine core (Fig. 1d, path (ii)). Under $ZnIn_2S_4$-photocatalytic conditions, the *in situ* generated radical $^{\bullet}NSO_2F$ undergoes addition with an alkene, achieving a polarity switch from electrophilic to nucleophilic character, followed by selective addition to the NFSAP salts in the system. The sequence culminates in remote C4-selective aminosulfonyl fluorination of the pyridine ring. By orchestrating a radical-relay pathway that inverts radical polarity, the strategy neutralizes the intrinsic mismatch between electrophilic radicals and electron-deficient pyridinium salts, offering a powerful new platform for the precision editing of heteroaromatic systems. Importantly, $ZnIn_2S_4$ demonstrates exceptional recyclability, maintaining high catalytic activity over at least five consecutive cycles. This feature effectively circumvents the principal limitations associated with catalyst recovery in previous photoredox systems, underscoring the promising potential of $ZnIn_2S_4$-based heterogeneous catalysis in sustainable organic synthesis.

Results and discussion

Reaction optimization

Our investigation began with the selection of *n*-butyl vinyl ether **1a** and *N*-fluorosulfamoyl pyridinium salt **2a** as model substrates to optimize the reaction conditions. The initial attempt employed $ZnIn_2S_4$ (10 mol%) as the photocatalyst and Na_3PO_4 (2.5 equiv.) as the base in CH_3OH, resulting in the formation of the desired product **3a** in only 14% yield (Table 1, entry 1). To improve the reaction efficiency, we systematically evaluated several solvents, including ethyl acetate (EA), dimethyl sulfoxide (DMSO), dichloromethane (DCM), 1,2-dichloroethane (DCE), acetonitrile (CH_3CN), and acetone (entries 2–7). Among these, acetone proved to be the most effective solvent, enhancing the yield of **3a** to 57% (entry 7). Subsequently, we investigated the influence of various bases on the reaction, testing a range of inorganic bases such as Na_2HPO_4, Na_2CO_3, $NaHCO_3$, and K_2HPO_4, along with organic bases like 1,4-diazabicyclo[2.2.2]octane (DABCO) and 1,8-diazabicyclo[5.4.0]undec-7-ene (DBU) (entries 8–13). Among these, $NaHCO_3$ emerged as the most efficient, significantly increasing the yield of **3a** to 71% (entry 10). We also optimized the reaction time and the amount of $NaHCO_3$, but these adjustments did not result in any further improvements in the yield (entries 14–20). Control experiments conducted in the absence of the photocatalyst, base, or light demonstrated a marked reduction in the yield of **3a**, thereby underscoring the indispensable roles of these components in facilitating the transformation (entries 21 and 22). The optimized reaction conditions are as follows: **1a** (0.1 mmol), **2a** (3.0 equiv.), $ZnIn_2S_4$

Table 1 Reaction optimization[a]

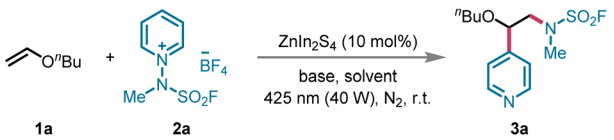

Entry	Solvent	Base	Time (h)	Yield (%)
1	CH_3OH	Na_3PO_4	3	14
2	EA	Na_3PO_4	3	8
3	DMSO	Na_3PO_4	3	Trace
4	DCM	Na_3PO_4	3	7
5	DCE	Na_3PO_4	3	7
6	CH_3CN	Na_3PO_4	3	20
7	Acetone	Na_3PO_4	3	57
8	Acetone	Na_2HPO_4	3	Trace
9	Acetone	Na_2CO_3	3	26
10	Acetone	$NaHCO_3$	3	71 (65)[b]
11	Acetone	$KHCO_3$	3	25
12	Acetone	DABCO	3	6
13	Acetone	DBU	3	N.D.
14	Acetone	$NaHCO_3$	1	63
15	Acetone	$NaHCO_3$	2	66
16	Acetone	$NaHCO_3$	4	58
17	Acetone	$NaHCO_3$	5	55
18[c]	Acetone	$NaHCO_3$	3	59
19[d]	Acetone	$NaHCO_3$	3	51
20[e]	Acetone	$NaHCO_3$	3	57
21[f]	Acetone	$NaHCO_3$	3	N.D.
22	Acetone	—	3	16

[a] Reaction conditions: **1a** (0.1 mmol), **2a** (3.0 equiv.), $ZnIn_2S_4$ (10 mol%) and solvent (0.1 M) were irradiated with 425 nm blue LED (40 W) at room temperature under N_2 atmosphere. Yields were given by ^1H NMR using 1,1,2,2-tetrachloroethane as an internal standard based on **1a**. [b] Isolated yield. [c] 1.5 equiv. of $NaHCO_3$. [d] 20 equiv. of $NaHCO_3$. [e] 3.0 equiv. of $NaHCO_3$. [f] No catalyst or no light.

(10 mol%) as the photocatalyst, $NaHCO_3$ (2.5 equiv.) as the base in acetone (0.1 M), under a nitrogen atmosphere, irradiated by blue light (425 nm) for 3 h.

Substrate scope

Having optimized the reaction conditions, we next explored the substrate scope, testing a wide range of alkenes and pyridines. The reaction showed excellent reactivity with electron-rich alkenes such as vinyl ethers and enamides, leading to efficient formation of β-aminopyridine derivatives with good C4-regioselectivity. Additionally, the transformation proved to be highly versatile, working well with aliphatic olefins of various chain lengths and cycloolefins, all of which showed good reactivity and compatibility (Scheme 1, **3a–3d**). Substrates bearing polar functional groups, including hydroxyl and chloro moieties, were also well tolerated, providing the desired products in good yields (**3e** and **3f**). The methodology was further applied to internal olefins, yielding the desired difunctionalized products **3g** and **3h** in moderate yields, albeit with slightly reduced efficiency. The approach also demonstrated significant flexibility, allowing the reaction to be extended to vinyl amides, formamides, and carbamates, resulting in products **3i–3l** in yields ranging from 37% to 61%. Moreover, pyridine derivatives with electron-donating groups such as 2-methyl, 2-methoxy, 2-phenyl, and 2-benzyl groups, as well as those with electron-withdrawing groups like 2-acetyl and 2-carboxymethyl (2-COOMe), all participated effectively in the reaction, yielding products **3m–3r** in moderate to excellent yields (35–68%). Even bicyclic pyridinium substrates gave good results, leading to products **3s** and **3t** in 96% and 69% yields. The lower yield of **3t** relative to **3s** is primarily ascribed to the more pronounced steric hindrance of the six-membered ring in **3t** compared to the five-membered ring in **3s**. This steric discrepancy between the two ring systems directly affects the spatial accessibility of the reaction site, thereby regulating the reaction efficiency (for details see SI). Notably, pyridine bearing a 2-thienyl group underwent concurrent sulfonyl fluorination at both heteroaromatic rings, resulting in product **3u**. It was also possible to expand the scope beyond the methyl substituent of *N*-fluorosulfamoyl pyridinium salt to include other groups, such as ethyl, resulting in the formation of the corresponding product **3v** with a yield of 65%. Afterward, we examined the *N*-methyl-free fluorosulfamoyl pyridinium salt under our standard photocatalytic conditions. This substrate was completely unreactive, which might be caused by the more negative reduction potential (for details, see the SI). To further evaluate the generality of our method, we investigated quinolinium and isoquinolinium salts. Quinolinium salts proved amenable to our standard conditions, delivering the remote quinoline sulfonyl fluoride product **3w** in 32% yield. In contrast, isoquinolinium salts failed to react, likely due to the lack of a suitable 4-position reaction site analogous to that in pyridinium and quinolinium systems (for details see the SI).

Late-stage functionalization has emerged as a groundbreaking approach in contemporary organic synthesis, providing a streamlined and direct pathway to architecturally intricate molecules with enhanced functionalities.[21] This rapid synthesis method for highly complex compounds opens up significant opportunities across various domains, such as drug discovery, advanced materials science, and cutting-edge molecular imaging technologies.[19a,22] To further underscore the synthetic versatility of this methodology, we investigated its application in modifying bioactive molecules. A diverse array of drug-derived alkenes, such as DL-menthol, nortropine, L-(−) borneol, and diacetone-D-glucose, were successfully employed as compatible substrates, yielding the desired products **3x–3aa** in moderate to high yields. Additionally, bioactive compounds, including ibuprofen piconol, nikethamide, nicotinyl alcohol, loratadine, and pyriproxyfen, were seamlessly integrated into the reaction, furnishing the corresponding products **3ab–3af**. To gain deeper insights into the reaction's sensitivity to varying conditions, we conducted a series of experiments to assess its reproducibility. We systematically varied a range of factors, including concentration, oxygen levels, water content, light intensity, and reaction scale, both positively and negatively relative to the standard reaction conditions (see SI for further details). As shown in Scheme 1, it revealed that the inert gas atmosphere had the most significant impact on reaction reproducibility, with optimal performance observed under a nitrogen atmosphere. The reaction also exhibited moderate sensitivity to light intensity. In contrast, factors such as concentration and humidity had minimal influence on the outcome.

Encouraged by the promising experimental results, we further extended our investigation by substituting *N*-fluorosulfamoyl pyridinium salts with *N*-benzene sulfonyl pyridinium salts to broaden the substrate scope of the heterogeneous photocatalytic system (Scheme 2). Notably, aminopyridylation of alkenes was achieved using a variety of *N*-aminopyridinium salts as dual aminating and pyridylating reagents. A wide range of alkyl (*e.g.*, butyl, ethyl, propyl, cyclohexyl), aryl, and distal chloro- or hydroxy-substituted alkenyl ethers, as well as cyclic enol ethers, underwent efficient transformations, leading to the corresponding target products **5a–5g** in moderate to good isolated yields. Notably, $NaHCO_3$ is also an effective base for this reaction, affording **5a** in 66% yield. Furthermore, vinyl amide derivatives, including *N*-vinylformamide, *N*-vinylacetamide, *N*-vinyl-2-pyrrolidone, and *N*-vinylcaprolactam, exhibited smooth reactivity under the established photochemical conditions, resulting products **5h–5k** in acceptable yields, respectively. Additionally, a series of pyridine substrates with *ortho*- and *meta*-substituents on the aromatic ring, such as methyl, methoxy, phenyl, benzyl, and ester groups, were well-tolerated, yielding the desired products **5n–5t** in yields ranging from 40% to 74%. Moreover, *N*-benzene sulfonyl pyridinium salts derived from 2,6-dimethylpyridine, cyclopenta[*b*]pyridine, and 5,6,7,8-tetrahydroquinoline were also viable substrates, successfully yielding the corresponding target compounds **5u–5w**.

To further validate the feasibility of the experimental approach, gram-scale synthesis was performed using a specially designed continuous-flow fixed-bed photoreactor (Fig. 2a). Leveraging the heterogeneous nature of $ZnIn_2S_4$ as a photocatalyst, the reactor was loaded with 0.25 g of $ZnIn_2S_4$ and 1.26 g

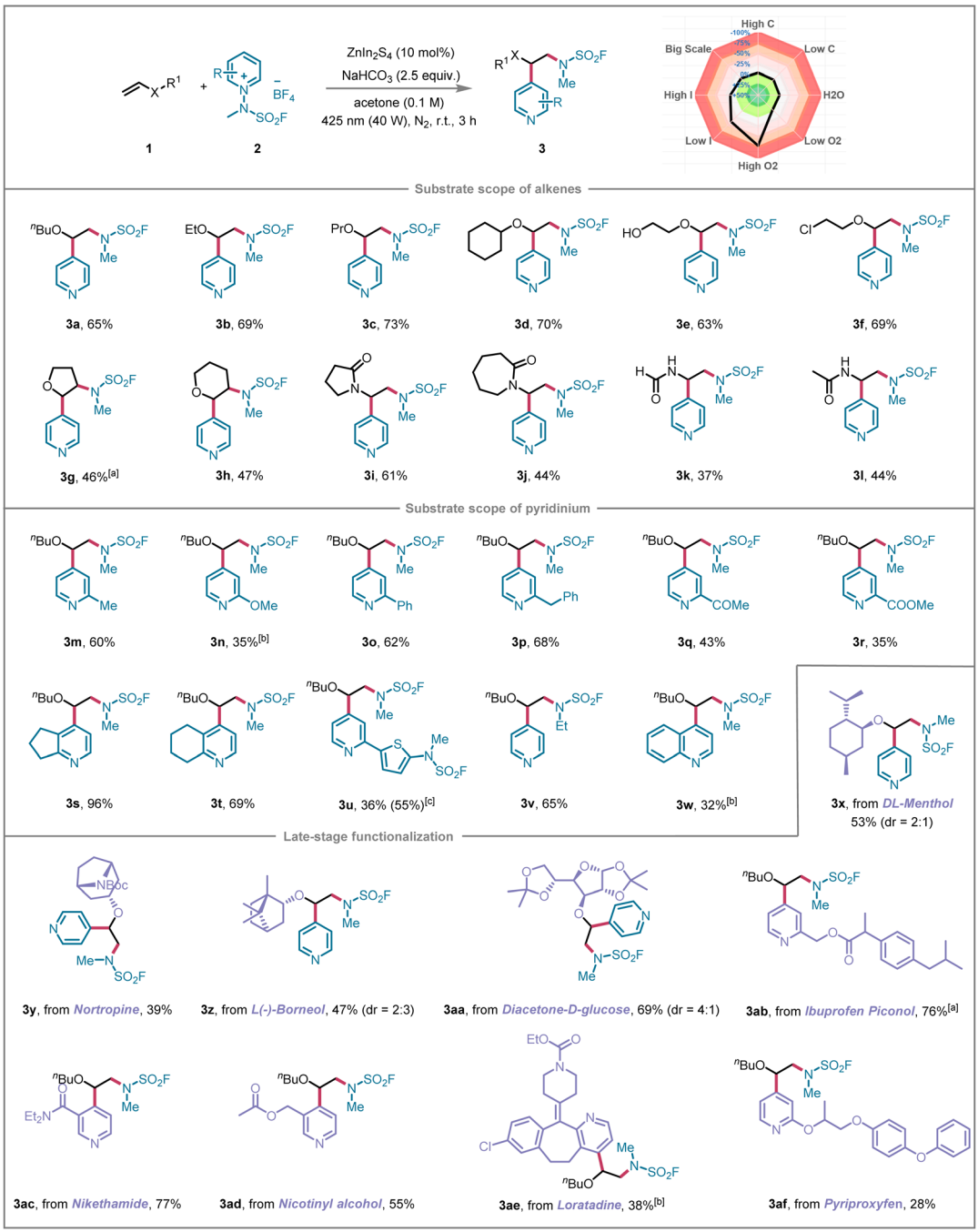

Scheme 1 The scope of alkenes and pyridinium salts. Reaction conditions: **1** (0.1 mmol), **2** (3.0 equiv.), $ZnIn_2S_4$ (10 mol%), $NaHCO_3$ (2.5 equiv.) and acetone (0.1 M) were irradiated with 40 W blue LED (425 nm) at room temperature under N_2 atmosphere for 3 h. [a]**1** (3.0 equiv.), **2** (0.1 mmol); [b]one-pot synthesis; [c]**1** (0.1 mmol), **2** (6.0 equiv.).

of $NaHCO_3$ supported on 50.00 g of commercially available silica microspheres (0.80 mm diameter). The system operated at a flow rate of 3.00 mL min^{-1}, corresponding to a residence time of 100 seconds within a 5.00 mL reactor volume, enabling efficient substrate conversion. Under simultaneous irradiation by two Kessil lamps (427 nm, 40 W each, providing an irradiance of 399.00 nW cm^{-2} at an 8.00 cm distance), a total of 1.14 g of the desired product **3a** was obtained, corresponding to a 65% yield from 6 mmol of substrate **1a**. These results confirm the efficacy of the photoreactor design for gram-scale synthesis employing $ZnIn_2S_4$ as the photocatalyst. The heterogeneous $ZnIn_2S_4$ photocatalyst could be conveniently recovered *via* centrifugation and reused for at least five cycles without appreciable loss of catalytic activity (Fig. 2b). Scanning electron microscopy (SEM) analysis of the recovered catalyst revealed no significant changes in overall morphology compared to the fresh material, indicating that the primary structural framework remained intact (Fig. S6). However, closer examination revealed small

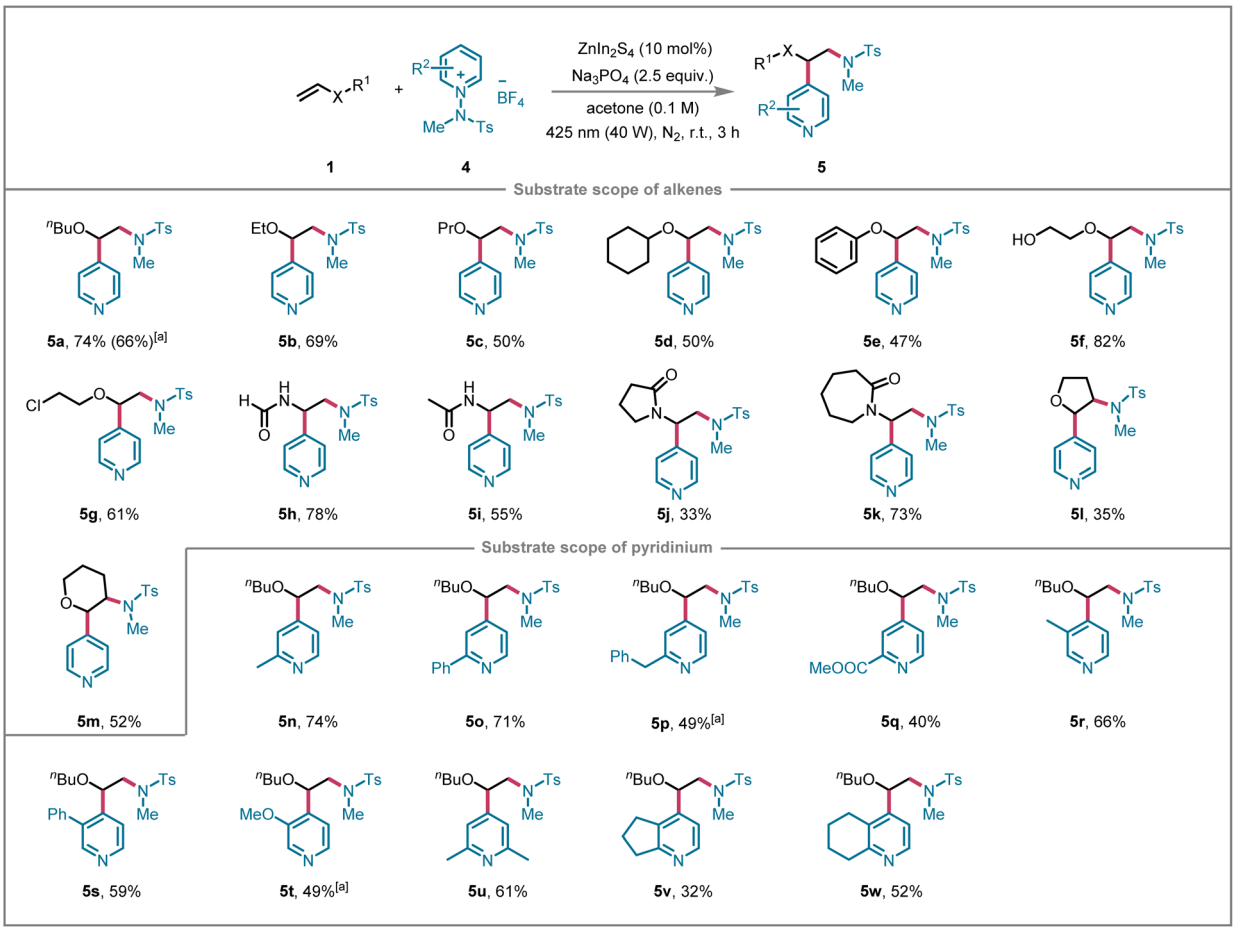

Scheme 2 The scope of alkenes and pyridinium salts. Reaction conditions: **1** (0.1 mmol), **2** (3.0 equiv.), $ZnIn_2S_4$ (10 mol%), Na_3PO_4 (2.5 equiv.), and acetone (0.1 M) were irradiated with 40 W blue LED (425 nm) at room temperature under N_2 atmosphere for 3 h. [a]$NaHCO_3$ as base.

particles on the surface of the recovered catalyst, likely arising from minor deposition of slight agglomeration, or adsorption of trace impurities. While the macroscopic structure is well preserved, these surface modifications could block active sites or disrupt light–matter interactions, which reasonably explains the slight decline in catalytic efficiency upon recycling. This excellent stability was further corroborated by XRD analysis, which showed that the crystal structure remained unchanged after catalytic cycling (Fig. 2c). Collectively, these findings underscore the robust recyclability and structural integrity of $ZnIn_2S_4$, highlighting its potential for sustainable applications.

The S(VI)–F bond in sulfamoyl fluorides exhibits exceptional synthetic versatility, serving as a crucial functional handle for a variety of SuFEx-mediated transformations. Therefore, we exploited the S–F bond of the synthesized compound **3a** to investigate efficient coupling reactions with diverse nucleophiles, including phenols, amines, and imidazole derivatives. As depicted in Fig. 2d, compound **3a** underwent nucleophilic substitution with alcohol-based pharmaceuticals such as estrone and sesamol, affording the corresponding products **6a** and **6b** in isolated yields of 70% and 39%, respectively. Moreover, imidazole and imidazole-containing pharmaceuticals, exemplified by detomidine hydrochloride, served effectively as nucleophiles, enabling the synthesis of products **6c** and **6d** with high isolated yields of 95% and 90%. Additionally, amine-containing drug molecules, such as phenylpiperazine and vortioxetine, reacted smoothly with the S(VI)–F bond, furnishing products **6e** and **6f** in excellent isolated yields of 95% and 96%, respectively. Furthermore, the synthetic utility of this approach was demonstrated through a base-mediated elimination of aminosulfonyl fluoride from compound **3a** in tetrahydrofuran, affording product **6g** with a yield of 58%. These results highlight the practical applicability of the S(VI)–F bond in facilitating diverse and efficient transformations, underscoring its significant potential in pharmaceutical chemistry and the development of novel therapeutic agents.

Mechanism

To gain deeper mechanistic insight into the reaction pathway, a comprehensive series of experiments was performed. Initial control experiments demonstrated that the addition of radical scavengers, specifically (2,2,6,6-tetramethylpiperidin-1-yl)oxyl (TEMPO) and 2,6-di-*tert*-butyl-4-methylphenol (BHT), under standard conditions completely inhibited the formation of the desired product, implicating radical intermediates in the transformation. Moreover, the introduction of $K_2S_2O_8$, serving

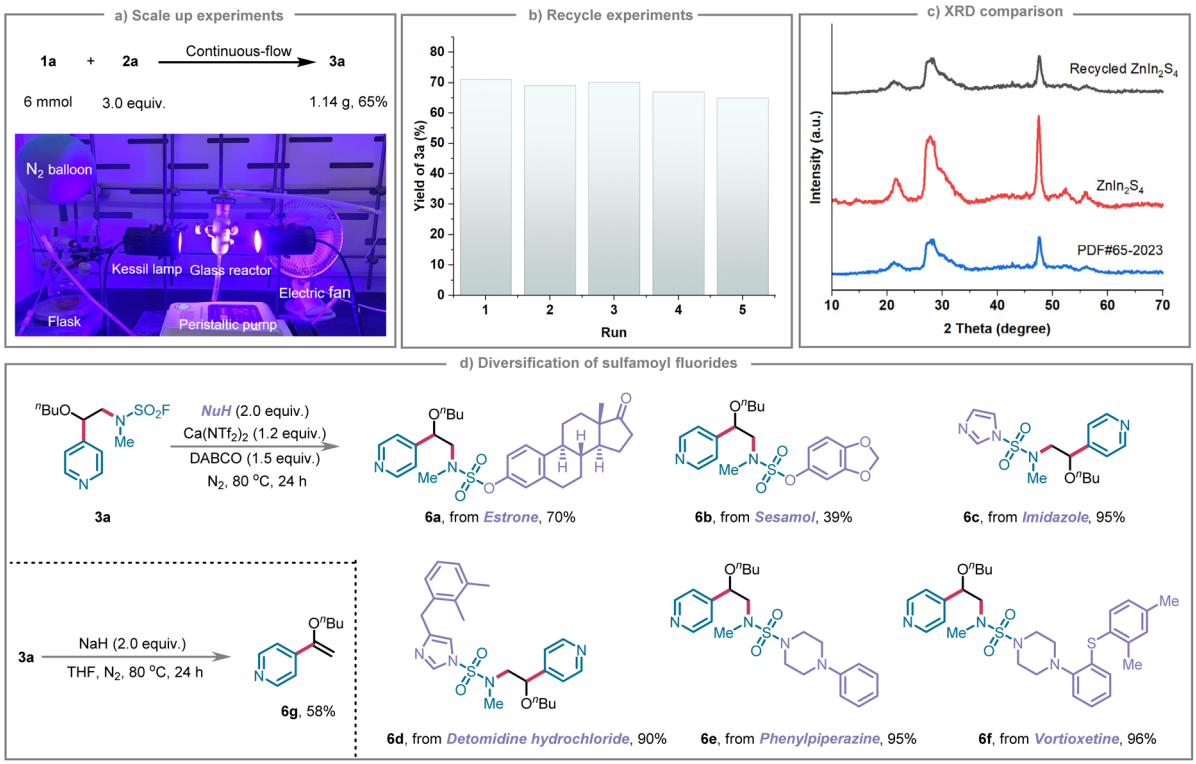

Fig. 2 Synthetic applications. (a) Scale-up experiments. (b) Recycle experiments. (c) XRD comparison of the recovered material, fresh $ZnIn_2S_4$ and PDF of $ZnIn_2S_4$. (d) Diversification of sulfamoyl fluorides.

as an electron scavenger, or ammonium oxalate, a hole scavenger, resulted in a marked reduction in the yield of product **3a**, underscoring the critical roles of both photogenerated electrons and holes derived from the semiconductor photocatalyst in facilitating the reaction progress. Furthermore, the addition of CuCl, a known single-electron transfer (SET) inhibitor, fully suppressed the reaction, highlighting the indispensable contribution of SET processes in this photocatalytic system (Fig. 3a). Stern–Volmer fluorescence quenching studies further substantiated the mechanistic hypothesis. The excited state of the photocatalyst underwent significant quenching in the presence of compound **2a**, while no appreciable quenching was detected with compound **1a**, suggesting a selective interaction likely involving SET between the photocatalyst and compound **2a** (Fig. 3b). To further elucidate the photochemical nature of the reaction, light "on–off" experiments were conducted. The reaction mixture was subjected to alternating cycles of LED irradiation, switching the light on and off every 20 minutes over a total period of 2 h. As depicted in Fig. 3c, product formation notably increased during the illumination intervals. Interestingly, increases in yield were also observed during the dark periods, implying the involvement of a radical chain propagation mechanism. This conclusion was further supported by the determination of a quantum yield of 14 (for details, see the SI), confirming that radical chain processes significantly contribute to the overall reaction pathway. Subsequently, to evaluate whether the pyridine species formed *in situ* could act as a substrate, mixtures of compound **2a** and 2-phenylpyridine were subjected to the standard conditions. The reaction proceeded exclusively with the pyridinium salt **2a**, whereas the pyridine derivative showed no reactivity, indicating that free pyridine does not participate in the transformation (Fig. 3d). The C-4 blocked experiment demonstrated that no desired product was obtained when the *N*-fluorosulfamoyl pyridinium salt, with a –OMe group at the C-4 position of the pyridine ring, was used (Fig. 3e). Cyclic voltammetry analysis showed that the reduction potential of compound **1a** ($E_{1/2}^{red} = -0.59$ V *vs.* Ag/AgCl) is appropriate for reduction by $ZnIn_2S_4$ (Fig. 3f and h). Finally, kinetic isotope effect (KIE) experiments were conducted to identify the rate-limiting step. The observed competitive KIE value of 1.7 suggests that C–H bond cleavage in *N*-fluorosulfamoyl pyridinium salts is not the rate-determining step of the overall transformation (Fig. 3g).

Based on our experimental results and consistent with previous studies,[11g] a plausible mechanistic pathway is proposed and illustrated in Fig. 3h. Upon visible light irradiation, the photocatalyst $ZnIn_2S_4$ is excited to generate electron–hole pairs, producing conduction band (CB) electrons and valence band (VB) holes. The photogenerated electrons in the CB undergo a single electron transfer (SET) process with pyridinium salts, resulting in the formation of free pyridines and sulfamoyl fluoride radical intermediate **A**. Subsequently, radical intermediate **A** adds to alkene **1a**, affording carbon-centered radical species **B**. Intermediate **B** then reacts with another equivalent of pyridinium salts to generate radical intermediate **C**. The base facilitates deprotonation of intermediate **C**, which

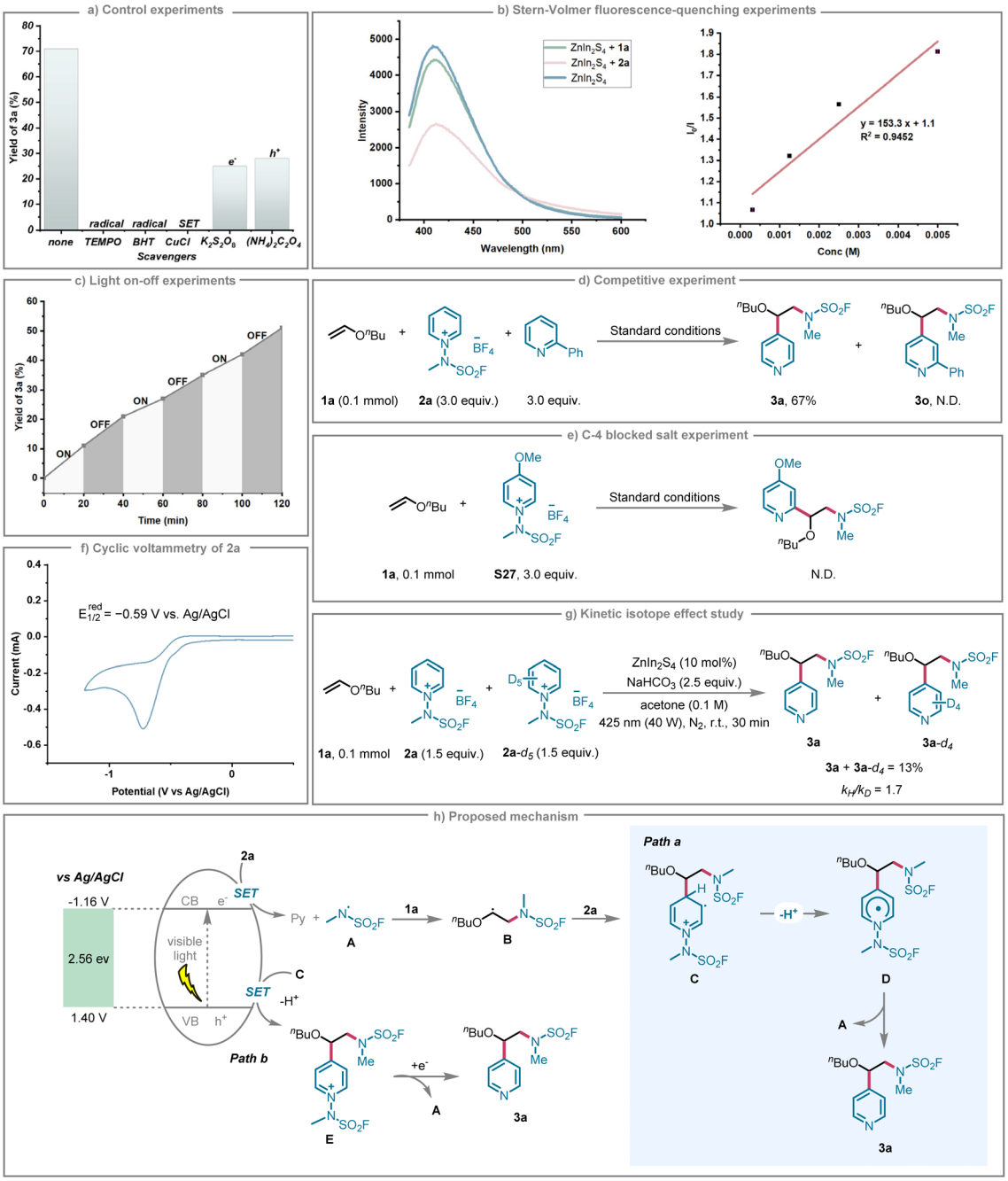

Fig. 3 Mechanism studies. (a) Control experiments. (b) Stern–Volmer fluorescence-quenching experiments. (c) Light on–off experiments. (d) Competitive experiment. (e) C-4 blocked salt experiment. (f) Cyclic voltammetry of **2a**. (g) Kinetic isotope effect study. (h) Proposed mechanism.

undergoes N-heteroatom bond cleavage to yield the final product while concurrently regenerating radical intermediate **A**, thus propagating the radical chain reaction. Moreover, to maintain catalyst turnover, an alternative pathway is proposed involving rearomatization and reduction *via* SET events within the photoredox catalytic cycle. In both pathways, the base plays a crucial role in the deprotonation steps essential for product formation.

In addition, we applied density functional theory (DFT) to calculate the factors governing the catalytic mechanism and regioselectivity during this transformation process. The photocatalytic cycle begins with excitation of the photocatalyst, followed by single-electron transfer to **2a**, generating the transient *N*-pyridyl radical **2a′**. Subsequent homolytic N–N bond cleavage releases pyridine while forming the key N-centered radical intermediate **A**. Computational analysis reveals this step has a moderate activation barrier of 6.40 kcal mol^{-1} and is strongly exergonic ($\Delta G = -23.00$ kcal mol^{-1}), rendering it effectively irreversible. For radical **A**, we identified two competing pathways: direct addition to either the alkene **1a** or to a second

equivalent of the pyridinium **2a**. Surprisingly, the attack on **2a** is both kinetically and thermodynamically unfavorable, requiring an energy barrier of 27.20 kcal mol^{-1} (*via* transition state **TSAp**) to form the putative intermediate **Bp**, which lies 12.10 kcal mol^{-1} higher in energy than **A** (Fig. 4, red dotted line). Computations reveal that the N-centered radical **A** instead adds smoothly to the olefin, surmounting a mere 8.10 kcal mol^{-1} barrier and releasing 10.80 kcal mol^{-1} to furnish radical **B**. We also examined the alternative α-position addition pathway; the corresponding transition state (**TSAa**) lies −11.1 kcal mol^{-1}, which is higher in energy than the transition state for the preferred pathway (**TSA**). The α C–N bond-forming route is energetically less favorable and does not compete significantly under the reaction conditions (Fig. 4, purple dotted line). For the reaction to proceed, alkyl radical **B** attacks the pyridinium salt species, first forming the unstable cationic radical intermediate **C** (a process with a low energy barrier), which then rapidly deprotonates to generate the more stable neutral radical **D**. This proton transfer step is expected to be barrierless in solution and was not subjected to explicit transition state optimization. The final step of the catalytic cycle involves the homolytic cleavage of the N–N bond, producing the target product **3a** while releasing radical intermediate **A**. Notably, theoretical calculations indicate that the difference in the energy barriers of the radical addition transition states from **B** to **C** is the primary controlling factor for the regioselectivity of the reaction. Although the two regioisomers **Cp** and **Co** exhibit nearly identical free energies (−30.10 *vs.* −29.00 kcal mol^{-1}, respectively), the transition state **TSBp** leading to the C4-intermediate **Cp** is energetically favored by 2.60 kcal mol^{-1} over the C2-pathway alternative, showing excellent agreement with the experimentally observed regioselectivity.

As depicted in Fig. 5a, the frontier orbitals reveal a decisive energy pattern: the SOMO of radical **A** sits at −8.81 eV, while the π and π* orbitals of the olefin lie at −6.42 and +0.25 eV, respectively; the analogous orbitals of **2a** are located at −9.21 and −3.50 eV. As highlighted in blue in Fig. 5a, the SOMO of radical **A** is energetically aligned with the occupied π orbital of olefin substrate **1a**, resulting in a stabilizing 2-orbital–3-electron interaction that renders the N-centered radical electrophilic toward the olefin. In contrast (red highlight, Fig. 5a), the positively charged pyridinium substrate **2a** exhibits substantially lowered orbital energies, with its π* orbital becoming the frontier orbital closest in energy to the SOMO of **A**. Consequently, these two MOs give a 2-orbital–1-electron interaction, and the radical acts as a nucleophile towards the pyridinium substrate. The interaction strength is controlled by both orbital overlap and the energy gap between participating orbitals: larger overlap and smaller energy gap lead to stronger interactions. The energy difference for olefin **1a** is 2.39 eV between interacting frontier orbitals, compared to 5.31 eV for the pyridinium substrate. Furthermore, the π orbital of the olefin exhibits greater localization than the π* orbital of the pyridinium, resulting in superior orbital overlap with the radical. Both factors synergistically favor radical–olefin interactions, rationalizing the observed transition state and intermediate energetics.

To establish the intrinsic reactivity of the pyridinium substrate, we conducted a comprehensive Fukui function analysis. The Fukui indices (f^0) for C2 and C4 positions of pyridinium salt **2a** were calculated as 0.074 and 0.154, respectively,

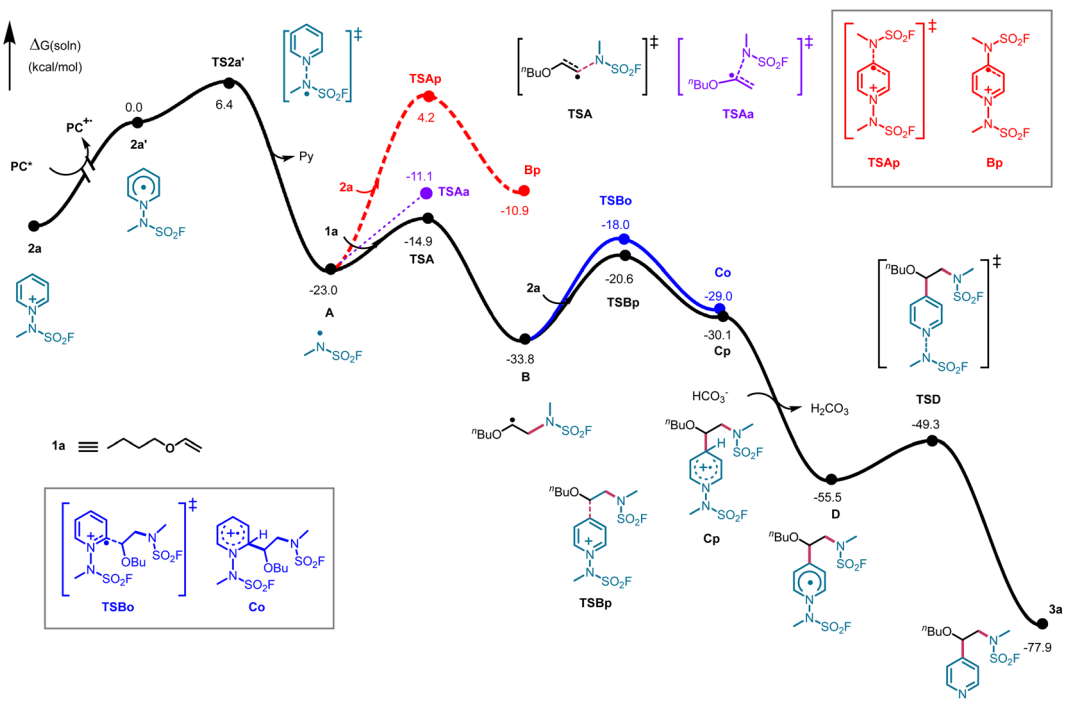

Fig. 4 Computational studies.

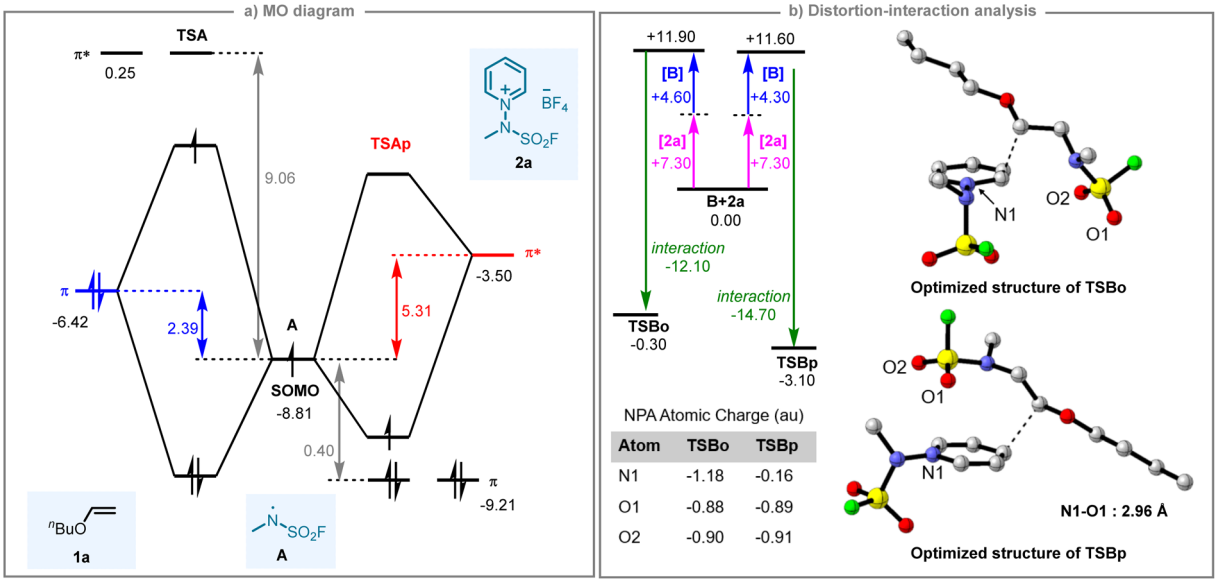

Fig. 5 MO diagram and distortion–interaction analysis. (a) Qualitative MO diagram of N-centered radical interaction with the enol ether **1a** or the pyridinium salt **2a**. Energies are given in eV. (b) Distortion–interaction analysis of TSBo and TSBp. [2a] and [B] indicate the structural distortion energy of radical and pyridinium fragments from the corresponding intermediates **2a** and **B** to each transition state geometry; Natural Population Analysis (NPA) was performed using the NBO 7.0 program to obtain NPA atomic charges.

where higher values indicate greater susceptibility to radical attack (for details, see SI). To understand how this intrinsic reactivity manifests in the transition states, natural population analysis (NPA) was performed using NBO 7.0 to map the atomic charge distributions (Fig. 5b). The analysis reveals two critical electronic distinctions between **TSBo** and **TSBp**. Regarding the pyridinium nitrogen (N1), **TSBo** shows a markedly negative charge (−1.18 a.u.), whereas **TSBp** exhibits a substantially less negative value (−0.16 a.u.) approaching electrostatic neutrality. For the sulfonyl oxygen atoms (O1, O2), both structures retain consistently electron-rich character (−0.88/−0.90 a.u. in **TSBo** and −0.89/−0.91 a.u. in **TSBp**). This charge distribution directly correlates with the observed regioselectivity: In **TSBp**, the weakly negative (electron-poor) N1 engages in favorable electrostatic attraction with the electron-rich sulfonyl O1, facilitated by a 2.96 Å noncovalent contact; this aligns with **TSBp**'s more stabilizing interaction energy (−14.70 kcal mol^{-1}). In contrast, the strongly negative N1 in **TSBo** (−1.18 a.u.) repels the negatively charged sulfonyl oxygens, and steric hindrance further blocks such contacts, consistent with its weaker interaction energy (−12.10 kcal mol^{-1}).

To quantify these energetic contributions, we performed a distortion–interaction analysis (Fig. 5b) by separating the pyridinium and alkyl fragments while maintaining their transition-state geometries. This decomposition reveals two critical components: the geometric distortion energy required to achieve the transition-state configurations (11.90 kcal mol^{-1} for **TSBo** *versus* 11.60 kcal mol^{-1} for **TSBp**) and the subsequent interaction energy between these distorted fragments (−12.10 kcal mol^{-1} for **TSBo** compared to −14.70 kcal mol^{-1} for **TSBp**). At the electronic energy level, this analysis identifies a 2.80 kcal mol^{-1} stabilization of **TSBp** relative to **TSBo**. Finally, to visualize the origin of the differential interaction energies, non-covalent interaction (NCI) analysis was conducted (Fig. S16). The NCI isosurfaces reveal that the enhanced stabilization in **TSBp** originates from a distinct O···N interaction between the sulfonyl oxygen and pyridinium nitrogen. In **TSBo**, steric hindrance from the adjacent alkyl chain obstructs this contact, as evidenced by the absence of an NCI isosurface in this region. This analysis provides direct visual evidence that the additional electrostatic attraction in **TSBp** is responsible for its lower interaction energy. Collectively, these results, from reactivity indices to electronic structure, energy decomposition, and visualization, confirm that the favorable electrostatic/non-covalent interaction in **TSBp**, enabled by its distinct electronic structure, is the key driver of the observed regioselectivity.

Conclusions

In conclusion, we have developed a pioneering heterogeneous visible-light photocatalytic system utilizing $ZnIn_2S_4$ for the efficient difunctionalization of alkenes with *N*-fluorosulfamoyl salts. This protocol facilitates the simultaneous incorporation of fluorosulfamoyl and pyridyl groups under mild conditions, delivering fluorosulfamoyl pyridine derivatives with broad substrate scope, excellent functional group tolerance, and moderate to good yields. The methodology significantly advances the practical application of the pyridine scaffold, widely prevalent in pharmaceuticals, by enabling rapid molecular complexity enhancement. Moreover, this heterogeneous photocatalytic system is also compatible with *N*-aminopyridinium salts, further showcasing its versatility. The exceptional recyclability and sustained catalytic performance of $ZnIn_2S_4$ over multiple cycles effectively address the challenge of

catalyst recovery encountered in previous homogeneous systems. The synthetic utility of this approach is further highlighted by the successful late-stage functionalization of complex bio-relevant molecules, and it leverages SuFEx click chemistry to diversify the resulting products. Overall, this work provides a practical and sustainable platform for constructing structurally complex fluorosulfamoyl and aminopyridyl derivatives, offering significant potential for future applications in pharmaceutical synthesis and chemical biology. Ongoing studies aim to further expand the scope and enhance the versatility of this photocatalytic strategy.

Author contributions

Kai Sun and Bing Yu designed and guided this project. Panjie Xiang, Kang Li, and Yunkai Zhang are responsible for the implementation of the experimental work. Kai Sun, Xiaolan Chen, and Xi Chen co-wrote the manuscript. Bing Yu and Lingbo Qu discussed the results and commented on the manuscript.

Conflicts of interest

There are no conflicts to declare.

Data availability

The data supporting this article have been included as part of the supplementary information (SI). Supplementary information: synthetic experiments, computational details, characterization data, and spectra. See DOI: https://doi.org/10.1039/d5sc08495d.

Acknowledgements

We acknowledge the financial support from the National Natural Science Foundation of China (21971224 and 22171249), the Science & Technology Innovation Talents in Universities of Henan Province (23HASTIT003), the 111 Project (D20003), Natural Science Foundation of Henan Province (242301420006, 252300421245), and Zhongyuan Leading Young Talents in Scientific and Technological Innovation.

Notes and references

1 J. Dong, L. Krasnova, M. G. Finn and K. B. Sharpless, *Angew. Chem., Int. Ed.*, 2014, **53**, 9430–9448.

2 (*a*) G. Laudadio, A. d. A. Bartolomeu, L. M. H. M. Verwijlen, Y. Cao, K. T. de Oliveira and T. Noël, *J. Am. Chem. Soc.*, 2019, **141**, 11832–11836; (*b*) M. Magre and J. Cornella, *J. Am. Chem. Soc.*, 2021, **143**, 21497–21502; (*c*) Q. Feng, T. He, S. Qian, P. Xu, S. Liao and S. Huang, *Nat. Commun.*, 2023, **14**, 8278.

3 (*a*) R. Xu, T. Xu, M. Yang, T. Cao and S. Liao, *Nat. Commun.*, 2019, **10**, 3752; (*b*) J. E. Erchinger, R. Hoogesteger, R. Laskar, S. Dutta, C. Hümpel, D. Rana, C. G. Daniliuc and F. Glorius, *J. Am. Chem. Soc.*, 2023, **145**, 2364–2374; (*c*) X. Nie, T. Xu, Y. Hong, H. Zhang, C. Mao and S. Liao, *Angew. Chem., Int. Ed.*, 2021, **60**, 22035–22042.

4 (*a*) S. D. Schimler, M. A. Cismesia, P. S. Hanley, R. D. J. Froese, M. J. Jansma, D. C. Bland and M. S. Sanford, *J. Am. Chem. Soc.*, 2017, **139**, 1452–1455; (*b*) G. Meng, T. Guo, T. Ma, J. Zhang, Y. Shen, K. B. Sharpless and J. Dong, *Nature*, 2019, **574**, 86–89; (*c*) M.-C. Giel, C. J. Smedley, E. R. R. Mackie, T. Guo, J. Dong, T. P. Soares da Costa and J. E. Moses, *Angew. Chem., Int. Ed.*, 2020, **59**, 1181–1186; (*d*) D.-D. Liang, D. E. Streefkerk, D. Jordaan, J. Wagemakers, J. Baggerman and H. Zuilhof, *Angew. Chem., Int. Ed.*, 2020, **59**, 7494–7500; (*e*) C. Liu, C. Yang, S. Hwang, S. L. Ferraro, J. P. Flynn and J. Niu, *Angew. Chem., Int. Ed.*, 2020, **59**, 18435–18441; (*f*) C. J. Smedley, Q. Zheng, B. Gao, S. Li, A. Molino, H. M. Duivenvoorden, B. S. Parker, D. J. D. Wilson, K. B. Sharpless and J. E. Moses, *Angew. Chem., Int. Ed.*, 2019, **58**, 4552–4556.

5 (*a*) S. Li, G. Li, B. Gao, S. P. Pujari, X. Chen, H. Kim, F. Zhou, L. M. Klivansky, Y. Liu, H. Driss, D.-D. Liang, J. Lu, P. Wu, H. Zuilhof, J. Moses and K. B. Sharpless, *Nat. Chem.*, 2021, **13**, 858–867; (*b*) B. Gao, L. Zhang, Q. Zheng, F. Zhou, L. M. Klivansky, J. Lu, Y. Liu, J. Dong, P. Wu and K. B. Sharpless, *Nat. Chem.*, 2017, **9**, 1083–1088; (*c*) R. W. Kulow, J. W. Wu, C. Kim and Q. Michaudel, *Chem. Sci.*, 2020, **11**, 7807–7812.

6 T. Hmissa, X. Zhang, N. R. Dhumal, G. J. McManus, X. Zhou, H. B. Nulwala and A. Mirjafari, *Angew. Chem., Int. Ed.*, 2018, **57**, 16005–16009.

7 (*a*) T. S.-B. Lou and M. C. Willis, *Nat. Rev. Chem.*, 2022, **6**, 146–162; (*b*) O. L. Symes, H. Ishikura, C. S. Begg, J. J. Rojas, H. A. Speller, A. M. Cherk, M. Fang, D. Leung, R. A. Croft, J. I. Higham, K. Huang, A. Barnard, P. Haycock, A. J. P. White, C. Choi and J. A. Bull, *J. Am. Chem. Soc.*, 2024, **146**, 35377–35389; (*c*) J. J. Rojas, R. A. Croft, A. J. Sterling, E. L. Briggs, D. Antermite, D. C. Schmitt, L. Blagojevic, P. Haycock, A. J. P. White, F. Duarte, C. Choi, J. J. Mousseau and J. A. Bull, *Nat. Chem.*, 2022, **14**, 160–169; (*d*) X. Wu, W. Zhang, G. Sun, X. Zou, X. Sang, Y. He and B. Gao, *Nat. Commun.*, 2023, **14**, 5168; (*e*) Y. Chen, G. B. Craven, R. A. Kamber, A. Cuesta, S. Zhersh, Y. S. Moroz, M. C. Bassik and J. Taunton, *Nat. Chem.*, 2023, **15**, 1616–1625; (*f*) A. Narayanan and L. H. Jones, *Chem. Sci.*, 2015, **6**, 2650–2659; (*g*) W. Chen, J. Dong, L. Plate, D. E. Mortenson, G. J. Brighty, S. Li, Y. Liu, A. Galmozzi, P. S. Lee, J. J. Hulce, B. F. Cravatt, E. Saez, E. T. Powers, I. A. Wilson, K. B. Sharpless and J. W. Kelly, *J. Am. Chem. Soc.*, 2016, **138**, 7353–7364.

8 (*a*) N. L. Frye, C. G. Daniliuc and A. Studer, *Angew. Chem., Int. Ed.*, 2022, **61**, e202115593; (*b*) P. Wang, H. Zhang, X. Nie, T. Xu and S. Liao, *Nat. Commun.*, 2022, **13**, 3370; (*c*) A. S. Barrow, C. J. Smedley, Q. Zheng, S. Li, J. Dong and J. E. Moses, *Chem. Soc. Rev.*, 2019, **48**, 4731–4758; (*d*) D. Zeng, W.-P. Deng and X. Jiang, *Natl. Sci. Rev.*, 2023, **10**, nwad123; (*e*) W. Zhang, H. Li, X. Li, Z. Zou, M. Huang, J. Liu, X. Wang, S. Ni, Y. Pan and Y. Wang, *Nat. Commun.*, 2022, **13**, 3515.

9 (*a*) C. M. Marshall, J. G. Federice, C. N. Bell, P. B. Cox and J. T. Njardarson, *J. Med. Chem.*, 2024, **67**, 11622–11655; (*b*) P. W. Xu, Z. Wang, S. M. Guo and A. Studer, *Nat. Commun.*, 2024, **15**, 4121; (*c*) H. Cao, Q. Cheng and A. Studer, *Science*, 2022, **378**, 779–785.

10 (*a*) X.-Y. Yu, J.-R. Chen and W.-J. Xiao, *Chem. Rev.*, 2021, **121**, 506–561; (*b*) M. Zhang, L. Liu, Y. Tan, Y. Jing, Y. Liu, Z. Wang and Q. Wang, *Angew. Chem., Int. Ed.*, 2024, **63**, e202318344; (*c*) T. Huang, P. G. Du, X. L. Cheng and Y. M. Lin, *J. Am. Chem. Soc.*, 2024, **146**, 24515–24525; (*d*) P. F. Zhong, J. L. Tu, Y. T. Zhao, N. Zhong, C. Yang, L. Guo and W. J. Xia, *Nat. Commun.*, 2023, **14**, 6530; (*e*) Y. Xie, R. Zhang, Z.-L. Chen, M. Rong, H. He, S. Ni, X.-K. He, W.-J. Xiao and J. Xuan, *Adv. Sci.*, 2024, **11**, 2306728; (*f*) J. Kim, M. Kim, J. Jeong and S. Hong, *J. Am. Chem. Soc.*, 2023, **145**, 14510–14518; (*g*) Y. M. Gao, J. Liu, C. Wei, Y. Li, K. Zhang, L. L. Song and L. C. Cai, *Nat. Commun.*, 2022, **13**, 7450; (*h*) J. Huang, Q. Gao, T. Zhong, S. Chen, W. Lin, J. Han and J. Xie, *Nat. Commun.*, 2023, **14**, 8292; (*i*) Z. Zhang, X. Lv, X. Mu, M. Zhao, S. Wang, C. Ke, S. Ding, D. Zhou, M. Wang and R. Zeng, *Nat. Commun.*, 2024, **15**, 4445; (*j*) M. Wu, Q. Jiang, Q. Tian, T. Guo, F. Cai, S. Tang, J. Liu and X. Wang, *CCS Chem.*, 2022, **4**, 3599–3608; (*k*) E. Le Saux, E. Georgiou, I. A. Dmitriev, W. C. Hartley and P. Melchiorre, *J. Am. Chem. Soc.*, 2023, **145**, 47–52; (*l*) C. Li, X. Li, J. Li, Z. Wang, D. Ouyang, N. Jiao and S. Song, *Nat. Synth.*, 2025, **5**, 36; (*m*) C. Li, Z. Yan, B. Wang, J. Li, W. Lyu, Z. Wang, N. Jiao and S. Song, *Chem*, 2024, **10**, 628–643; (*n*) J. Zhang, G. Wu, Y. Zhao, X. Liu, H. Zhu, A. Studer, X. Qi and Q. Cheng, *Nat. Synth.*, 2025, **5**, 27.

11 (*a*) F.-S. He, S. Ye and J. Wu, *ACS Catal.*, 2019, **9**, 8943–8960; (*b*) M. Vellakkaran, T. Kim and S. Hong, *Angew. Chem., Int. Ed.*, 2022, **61**, e202113658; (*c*) S. Jung, S. Shin, S. Park and S. Hong, *J. Am. Chem. Soc.*, 2020, **142**, 11370–11375; (*d*) M. Kim, Y. Koo and S. Hong, *Acc. Chem. Res.*, 2022, **55**, 3043–3056; (*e*) Y. Moon, W. Lee and S. Hong, *J. Am. Chem. Soc.*, 2020, **142**, 12420–12429; (*f*) J. Kim, Y.-E. Kim and S. Hong, *Angew. Chem., Int. Ed.*, 2024, **63**, e202409561; (*g*) Y. Moon, B. Park, I. Kim, G. Kang, S. Shin, D. Kang, M.-H. Baik and S. Hong, *Nat. Commun.*, 2019, **10**, 4117.

12 J. J. A. Garwood, A. D. Chen and D. A. Nagib, *J. Am. Chem. Soc.*, 2024, **146**, 28034–28059.

13 (*a*) A. Thakur, S. S. Gupta, Sumit, Sachin and U. Sharma, *Org. Lett.*, 2024, **26**, 8515–8520; (*b*) Y.-L. Su, G.-X. Liu, L. De Angelis, R. He, A. Al-Sayyed, K. S. Schanze, W.-H. Hu, H. Qiu and M. P. Doyle, *ACS Catal.*, 2022, **12**, 1357–1363; (*c*) H. Im, W. Choi and S. Hong, *Angew. Chem., Int. Ed.*, 2020, **59**, 17511–17516; (*d*) J. Q. Buquoi, J. M. Lear, X. Gu and D. A. Nagib, *ACS Catal.*, 2019, **9**, 5330–5335.

14 H. Li, X. Zhang, Z. Wang, C. Sun, M. Huang, J. Liu, Y. Li, Z. Zou, Y. Pan, W. Zhang and Y. Wang, *Org. Lett.*, 2024, **26**, 6714–6719.

15 P. Wang, L. Lin, Y. Huang, H. Zhang and S. Liao, *Angew. Chem., Int. Ed.*, 2024, **63**, e202405944.

16 T. Xiong, Q.-L. Chen, Z.-Y. Zhang, G. Lu and J. Weng, *ACS Catal.*, 2024, **14**, 12082–12092.

17 (*a*) W. Ou, G. Zhang, J. Wu and C. Su, *ACS Catal.*, 2019, **9**, 5178–5183; (*b*) J. Dong, Z. Wang, X. Wang, H. Song, Y. Liu and Q. Wang, *Sci. Adv.*, 2019, **5**, eaax9955; (*c*) J. Djossou, A. Aloia, L. Capaldo, D. D. Snabilié, M. Regnier, J. H. A. Schuurmans, A. Monopoli, B. d. Bruin and T. Noël, *Angew. Chem., Int. Ed.*, 2025, **64**, e202508710.

18 (*a*) Y. Cai, Y. Tang, L. Fan, Q. Lefebvre, H. Hou and M. Rueping, *ACS Catal.*, 2018, **8**, 9471–9476; (*b*) I. Ghosh, J. Khamrai, A. Savateev, N. Shlapakov, M. Antonietti and B. König, *Science*, 2019, **365**, 360–366; (*c*) Z. Teng, Z. Zhang, H. Yang, Q. Zhang, T. Ohno and C. Su, *Sci. Adv.*, 2024, **10**, eadl5432; (*d*) R.-N. Ci, C. Huang, L.-M. Zhao, J. Qiao, B. Chen, K. Feng, C.-H. Tung and L.-Z. Wu, *CCS Chem.*, 2022, **4**, 2946–2952.

19 (*a*) J.-J. Li, J.-Y. Liu, S.-Y. Gao, X. Yang and R. Cao, *J. Am. Chem. Soc.*, 2025, **147**, 21754–21763; (*b*) P. Nayek, B. Pal and P. Mal, *ACS Catal.*, 2025, **15**, 15519–15558.

20 (*a*) Y. Wu, Z. Liu, Y. Li, J. Chen, X. Zhu and P. Na, *Chin. J. Catal.*, 2019, **40**, 60–69; (*b*) D. Liu, S. Chen, Y. Zhang, R. Li and T. Peng, *Appl. Catal., B*, 2023, **333**, 122805; (*c*) S. Su, G. Lv, X. Zou, J. Wang, C. Zhou, Y. Chen, J. Shen, Y. Shen and Z. Liu, *Green Chem.*, 2023, **25**, 9262–9271; (*d*) Z. Sun, Y. Tan, X. Shi, B. Li, X. Wang, J. Wen, L. Huang and W.-M. Lau, *ACS Sustainable Chem. Eng.*, 2024, **12**, 1051–1061.

21 (*a*) C.-L. Ji, Y.-N. Lu, S. Xia, C. Zhu, C. Zhu, W. Li and J. Xie, *Angew. Chem., Int. Ed.*, 2025, **64**, e202423113; (*b*) J. Xu, J. Cao, X. Wu, H. Wang, X. Yang, X. Tang, R. W. Toh, R. Zhou, E. K. L. Yeow and J. Wu, *J. Am. Chem. Soc.*, 2021, **143**, 13266–13273; (*c*) S. Tong, K. Li, X. Ouyang, R. Song and J. Li, *Green Synth. Catal.*, 2021, **2**, 145–155; (*d*) Q. Shi, X.-W. Kang, Z. Liu, P. Sakthivel, H. Aman, R. Chang, X. Yan, Y. Pang, S. Dai, B. Ding and J. Ye, *J. Am. Chem. Soc.*, 2024, **146**, 2748–2756.

22 (*a*) S. Y. Guo, Y. P. Liu, J. S. Huang, L. B. W. He, G. C. He, D. W. Ji, B. S. Wan and Q. A. Chen, *Nat. Commun.*, 2024, **15**, 6102; (*b*) X.-Y. Chen, Y.-N. Li, Y. Wu, J. Bai, Y. Guo and P. Wang, *J. Am. Chem. Soc.*, 2023, **145**, 10431–10440; (*c*) S. Xu, Y. Ping, M. Xu, G. Wu, Y. Ke, R. Miao, X. Qi and W. Kong, *Nat. Chem.*, 2024, **16**, 2054–2065.